Green-function approach to transport through a gate-surrounded Si nanowire with impurity scattering

Jung Hyun Oh and D. Ahn*
Institute of Quantum Information Processing and Systems, University of Seoul, Seoul 130-743, Korea

Y. S. Yu
Department of Information and Control Engineering, Hankyong National University, Anseong 456-749, Korea

S. W. Hwang
School of Electrical Engineering, Korea University, Seoul 136-701, Korea

(Received 14 June 2007; revised manuscript received 15 October 2007; published 14 January 2008)

We investigate the transport properties of gate-surrounded Si nanowires using a nonequilibrium Green's function technique. By taking into account the ionized-impurity scattering, we calculate Green's functions self-consistently and examine the effects of ionized-impurity scattering on the electron densities and the currents. For nanoscale Si wires, it is found that, due to the impurity scattering, the local density of state profiles lose its interference oscillations as well as is broadened and shifted. In addition, the impurity scattering gives rise to a different transconductance as a function of temperature and impurity scattering strength when compared with that in the absence of impurity scattering.

DOI: 10.1103/PhysRevB.77.035313 PACS number(s): 72.10.Fk, 73.21.Hb, 73.23.−b

I. INTRODUCTION

A study of a ballistic electron transport in nanodevices has been an interesting field of research.[1–4] Recently, a Si nanowire with a length comparable to the de Broglie wavelength of carriers is realized by advanced nanofabrication technique.[5,6] The cross-sectional area of Si nanowires was designed to show well-separated transverse modes and electrons confined to the wire are expected to suffer from a minimal amount of impurity scattering. These properties make the Si nanowires good candidates for the study of ballistic quantum transport. In addition, the potential distribution within the wire is controllable by a metallic gate around the wire. This provides an additional degree of freedom on the current flow through the device and one would expect that the basic transistor action is possible for a Si nanowire. As a result, the gate-surrounded Si wire may shed the light on one-dimensional structures for future transistor applications.

It is desirable experimentally to make the Si wires as intrinsic as possible. However, to populate the wires with carriers, it is necessary to define source and drain regions where ionized dopants are placed. These dopants scatter free carriers and the elastic impurity scattering cannot be avoided in those regions. Thus, in order to understand transport in the wires, a quantitative treatment of the ionized-impurity scattering will be important. Several theoretical works were done to investigate the effects of ionized-impurity scattering on one-dimensional electron gas, and revealed their effects on the electronic structure.[7] Most of these studies were for uniformly doped or remote-impurity systems[8,9] and adopted empirical models based on the so-called Büttiker probes for simulating the device.[10,11] The empirical methods are appealing due to relatively simple implementation but the methods often require parameters that need to be adjusted using more rigorous calculations or values from experiments.

In this work, we take into account the ionized-impurity scattering in simulating the gate-surrounded nanowire using nonequilibrium Green-function approach. By averaging the Green's function over impurity configurations and expanding the arising term perturbatively, we treat the impurity scattering within the self-consistent Born approximation and apply the formula to the Si nanowire as realized in Ref. 6. Since the impurity-scattering strength is a single parameter for the system, the method provides an efficient way to understand current-voltage characteristics and compare them with the experimental results.

II. CALCULATION METHOD

A. Hamiltonian

To see the effects of the impurity scattering clearly, we consider a simple geometry of a quantum wire as in Fig. 1. An infinitely long cylindrical Si wire consists of intrinsic channel and heavily doped source and drain regions. A metallic gate extended over a length of L_G is rolled round the intrinsic region and they are separated from each other by a SiO_2 layer with a width t_{ox}. For simplicity, we assume that the Si wire is grown along the crystal [001] axis(chosen as

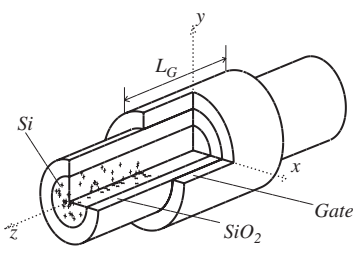

FIG. 1. We plot a schematic diagram of a cylindrical Si wire simulated in this work which is oriented along the [001] direction. The Si wire surrounded with the gate is assumed to be intrinsic and separate the source and drain regions where ionized dopants are distributed.

the z direction in the figure) and the doping profile of $N_D(\mathbf{r})$ in the source and drain regions is symmetric about the z axis so that we can utilize the circular symmetry.

Then, electrons in the Si wire are governed by the effective-mass Hamiltonian which is given by

$$\hat{H} = \int \hat{\psi}^*(\mathbf{r}) \left\{ -\frac{\hbar^2}{2}\left(\frac{1}{m_x}\frac{d^2}{dx^2} + \frac{1}{m_y}\frac{d^2}{dy^2} + \frac{1}{m_z}\frac{d^2}{dz^2}\right) + U(\mathbf{r}) + U_{imp}(\mathbf{r}) \right\} \hat{\psi}(\mathbf{r}) d\mathbf{r}. \quad (1)$$

Above Hamiltonian describes electrons in six different valleys depending on their effective masses. For instance, if $m_x = m_z = 0.19m$, transverse mass, and $m_y = 0.95m$, longitudinal mass of Si, the Hamiltonian represents electrons in the [010] valley, etc. Here, $U(\mathbf{r})$ is the macroscopic potential energy resulted from both band discontinuity among the materials, and the Coulomb contribution from external charges. The Coulomb part is determined by Poisson's equation

$$-\nabla^2 U(\mathbf{r}) = \frac{e^2}{\epsilon_{\mathrm{Si}}}\{N_D(\mathbf{r}) - n_{el}(\mathbf{r})\}, \quad (2)$$

when we know the electron distribution $n_{el}(\mathbf{r})$. $U_{imp}(\mathbf{r})$ describes the impurity potential energy from the ionized dopants. In this work, we assume that the impurity potentials are short ranged but still vary slowly in the atomic scale. As a result, different valley modes are not coupled by the impurity potential and can be solved independently.

Since the device has the circular symmetry, it is convenient to express the Hamiltonian in terms of the basis diagonalizing the radial motion. We choose the basis satisfying the following Schrödinger equation:

$$\left[-\frac{\hbar^2}{2}\left(\frac{1}{m_x}\frac{d^2}{dx^2} + \frac{1}{m_y}\frac{d^2}{dy^2}\right) + U_B(\vec{\rho}) \right] |\chi_l\rangle = \epsilon_l |\chi_l\rangle, \quad (3)$$

where $\vec{\rho}$ is radial coordinates (x,y) and $U_L(\vec{\rho}) = U(\vec{\rho}, \pm\infty)$ is a potential energy at $z = \pm\infty$, i.e., in the deep source and drain regions. Then, we expand the field operator $\hat{\psi}(\mathbf{r})$ as

$$\hat{\psi}(\mathbf{r}) = \sum_{ml} \hat{b}_{lm} \chi_l(\vec{\rho}) \psi(z_m), \quad (4)$$

where we discretize the longitudinal coordinates with a spacing of a and $\psi(z_m)$ is tight-binding basis at the mth node $(z_m = ma, m = -\infty, \ldots, \infty)$.

Using Eq. (4) and a finite difference approximation, one can express the Hamiltonian of Eq. (1) as

$$\hat{H} = \sum_{lml'm'} \hat{b}^\dagger_{lm} [\mathbf{H}_{lm:l'm'} + \mathbf{v}_{lm:l'm'} + \langle \chi_l | U_{imp}(\vec{\rho}, z_m) \times |\chi_{l'}\rangle] \delta_{mm'}] \hat{b}_{l'm'}. \quad (5)$$

Here, the first term describes motion along the longitudinal direction for each transverse mode and its elements are given by

$$\mathbf{H}_{lm:l'm'} = [\delta_{m,m'}(\epsilon_{lm} + 2t_H) - t_H(\delta_{m,m'+1} + \delta_{m,m'-1})]\delta_{ll'}$$

with $\epsilon_{ml} = \epsilon_l + \langle \chi_l | U(\vec{\rho}, z_m) - U_L(\vec{\rho}) | \chi_l \rangle$ and the hopping energy of $t_H = \hbar^2 / 2m_z a^2$ (hereafter, we use bold characters to denote a matrix displayed on the basis $\{\chi_l \psi_m\}$). The $\mathbf{v}$ matrix in Eq. (5) accounts for the deviated potential distribution from that of deep source and drain regions. As a result, it gives rise to the hybridization among transverse modes as

$$\mathbf{v}_{lm:l'm'} = [\langle \chi_l | U(\vec{\rho}, z_m) - U_L(\vec{\rho}) | \chi_{l'} \rangle \ (1 - \delta_{l,l'})\delta_{mm'}. \quad (6)$$

The last term in Eq. (5) is a contribution from the impurity potential.

B. Impurity-averaged Green's function

Now we formulate nonequilibrium Green's functions for the Hamiltonian of Eq. (5). In order to take into account the impurity scattering, we consider a number of impurity configurations rather than a particular distribution, and average the Green's functions over the configurations. For this we adopt the Schwinger-Keldysh technique.[12] According to the scheme, the impurity average gives rise to the quadratic interaction in the action, and we expand it perturbatively to obtain the one-particle irreducible self-energy $\mathbf{\Sigma}^{imp}$. Here, we restrict our attention to the first order diagram and treat it self-consistently, which is referred to as the self-consistent Born approximation.[8,9,13,14]

The impurity-averaged Green's function $\mathbf{G}$ can be obtained through the Dyson's equation

$$\mathbf{G}(E) = \mathbf{g}(E) + \mathbf{g}(E)\mathbf{\Sigma}^{imp}(E)\mathbf{G}(E), \quad (7)$$

where $\mathbf{g}$ is the impurity-free Green's function (in fact, the bold characters in this case represent enlarged matrices for taking into account the Keldysh space. However, we keep the notation in the meanwhile because it recovers an original size when we specify its components explicitly in the Keldysh space). The corresponding self-energy from the impurity scattering depends on its Green's functions again through the relation

$$\mathbf{\Sigma}^{imp}_{lm:l'm'}(E) = \sum_{l_1 m_1 l_2 m_2} S_{lml'm':l_1 m_1 l_2 m_2} \mathbf{G}_{l_1 m:l_2 m}(E), \quad (8)$$

with

$$S_{lml'm':l_1 m_1 l_2 m_2} = \tfrac{1}{2}\langle\langle \chi_l \psi_m | U_{imp}(\mathbf{r}) | \chi_{l_1} \psi_{m_1}\rangle \langle \chi_{l_2} \psi_{m_2} | U_{imp}(\mathbf{r}') \times |\chi_{l'} \psi_{m'}\rangle\rangle_{av}. \quad (9)$$

Here, $\langle \cdots \rangle_{av}$ denotes a configuration average and results in the correlation between impurity potentials. As for impurity potential in one-dimensional systems, it is known that screening properties are drastically different from in three-dimensional ones due to a low dielectric constant of a surrounding material.[15] Nevertheless, we model fluctuating impurity potentials with a δ-correlated function, as in a three-dimensional system, for simplicity;

$$\langle U_{imp}(\mathbf{r}) U_{imp}(\mathbf{r}') \rangle_{av} = n_D(\mathbf{r}) u_0^2 l_s^3 \delta(\mathbf{r} - \mathbf{r}'). \quad (10)$$

Here, $n_D(\mathbf{r}) = N_D(\mathbf{r}) / N_0$ is a normalized doping profile with respect to the atomic density N_0 of Si. Moreover, the impu-

rity potential strength is expressed with the impurity potential amplitude of u_0 and a screening length $l_s=4$ Å, which is approximately equal to the Thomas-Fermi screening length in the bulk Si at carrier density of $1\times10^{20}/\mathrm{cm}^3$. Accordingly, the expansion coefficient in Eq. (8) becomes

$$S_{lml'm':l_1m_1l_2m_2} = \frac{u_0^2 l_s^3}{2a}\delta_{mm'}\delta_{m_1m_2}\delta_{mm_1}\langle\chi_l|\chi_{l_1}(\rho)n_D(\rho,z_m)\chi^*_{l_2}(\rho) \times|\chi_{l'}\rangle. \tag{11}$$

It is noted that the short-ranged potential is diagonal for longitudinal basis $\{\psi_m\}$ but not for transverse modes $\{\chi_l\}$. This means that transverse modes are mixed to each other through the impurity scattering.

For a given $\mathbf{\Sigma}^{imp}$, in order to solve the Dyson equation of Eq. (7), we should take care of open boundaries in our problem, i.e., the infinite number of nodes along the longitudinal direction $(m=-\infty,\ldots,\infty)$. For this, we follow the conventional approach where the device is partitioned into the system being in nonequilibrium and reservoirs.[16] Since the source and drain regions are extended semi-infinitely, we confine our attention to the portion of the system near the gate where physical properties are thought to be deviated from those of deep source and drain regions. We designate the portion by longitudinal indices $m=(0,1,\ldots,M-1)$. Thus, nodes for $m<0$ $(m\geqslant M)$ represent the source (the drain) being in equilibrium with the chemical potential μ_S (μ_D).

In the source and drain reservoirs, we assume that the self-energy $\mathbf{\Sigma}^{imp}$ is independent of longitudinal coordinates m because they are sufficiently far from the gate region where the potential distribution is uneven. Within this assumption, the Schrödinger equation is easily solved and equilibrium Green's functions $\mathbf{G}(E)$ with corresponding self-energies are calculated straightforwardly. In the Appendix, we illustrate their simple expressions.

Now, we focus on the device region, i.e., nodes ranging $0\leqslant m<M$ where one expects a nonequilibrium situation for different chemical potentials of μ_S and μ_D. The Green's functions are obtained by truncating the matrix equation of Eq. (7) within longitudinal indices of $0\leqslant m<M$. Instead, the truncation introduces an additional self-energy $\tilde{\mathbf{\Sigma}}$ to the Dyson equation owing to the coupling of the source and drains, and a total self-energy becomes $\mathbf{\Sigma}=\tilde{\mathbf{\Sigma}}+\mathbf{\Sigma}^{imp}$. Here, the self-energy $\tilde{\mathbf{\Sigma}}(E)$ reads

$$\tilde{\mathbf{\Sigma}}_{lm:l'm'}(E) = t_H^2\delta_{mm'}[\delta_{m,0}\mathbf{G}_{l(-1):l'(-1)}(E)|_{\mu=\mu_S} + \delta_{m,M-1}\mathbf{G}_{lM:l'M}(E)|_{\mu=\mu_D}], \tag{12}$$

where the subscripts of $\mu=\mu_{S,D}$ denote that each equilibrium Green's function is determined by different chemical potentials of $\mu_S=\mu_0-eV_S$ and $\mu_D=\mu_0-eV_D$ accounting for applied voltages, V_S and V_D at each reservoir, respectively.

Solutions of the Dyson equation are obtained by inverting the matrix equation (7). Firstly, its retarded component is calculated as

$$\mathbf{G}^R(E) = [(\mathbf{g}^R)^{-1} - \mathbf{\Sigma}^R]^{-1}. \tag{13}$$

Here, $\mathbf{g}^R(E)=[E\mathbf{1}-\mathbf{H}-\mathbf{v}]^{-1}$ is the free-particle Green's function and $\mathbf{\Sigma}^R(E)=\tilde{\mathbf{\Sigma}}^R(E)+\mathbf{\Sigma}^{imp,R}(E)$ is a retarded component of the self-energy. Detailed form of $\tilde{\mathbf{\Sigma}}^R(E)$ is given in the Appendix. Whereas, the term of $\mathbf{\Sigma}^{imp,R}(E)$ depends on diagonal components of its own Green's function, as indicated by Eq. (8). Thus, we should solve the above matrix equation self-consistently.

With the obtained $\mathbf{G}^R$ and its Hermitian conjugate $\mathbf{G}^A$, the Keldysh components of the Green's function and the self-energy become

$$\mathbf{G}^K(E) = \mathbf{G}^R(E)\mathbf{\Sigma}^K(E)\mathbf{G}^A(E) \tag{14}$$

and

$$\mathbf{\Sigma}^K(E) = \tilde{\mathbf{\Sigma}}^K(E) + \mathbf{\Sigma}^{imp,K}(E), \tag{15}$$

respectively. According to Eq. (12), the self-energy contributed from the the source and drain coupling is obtained as

$$\tilde{\mathbf{\Sigma}}^K_{lm:l'm'}(E) = \tilde{\mathbf{\Sigma}}^C_{lm:l'm'}(E)\left[\delta_{m,0}\tanh\left(\frac{E-\mu_S}{2k_BT}\right) + \delta_{m,M-1}\tanh\left(\frac{E-\mu_D}{2k_BT}\right)\right], \tag{16}$$

with $\tilde{\mathbf{\Sigma}}^C(E)=\tilde{\mathbf{\Sigma}}^R(E)-\tilde{\mathbf{\Sigma}}^A(E)$, the correlated component of the self-energy. However, for the Keldysh component of the impurity-induced self-energy $\mathbf{\Sigma}^{imp,K}(E)$ the result is not given in a closed form and should be calculated self-consistently as in the case of the retarded one via Eqs. (8) and (14).

C. Electron density and current

The ensemble average of $n_{lm}=\langle b^\dagger_{lm}b_{lm}\rangle$ gives local electron density of the device and, consequently, the electron density distribution in Eq. (2) becomes $n_{el}(\vec{r})=\Sigma_{lm}n_{lm}\chi_l(\vec{\rho})\psi(z_m)$. From the generating functional technique as in Ref. 17, one can express the local electron density with the calculated Green's functions. The result reads

$$n_{lm} = \frac{1}{2a}\left[1-\frac{i}{2\pi}\int_{-\infty}^{\infty}dE\mathbf{G}^K_{lm:lm}(E)\right] = \mathrm{tr}\int_{-\infty}^{\infty}dE[\mathbf{f}_{FD}(E)\mathbf{D}(lm{:}E)]. \tag{17}$$

Here, in the second line we use the functional form of Fermi-Dirac distribution $\mathbf{f}_{FD}(E)$ and the density-of-states $\mathbf{D}(lm:E)$ for the resemblance with equilibrium results. Since the device is in nonequilibrium condition, two functions are given in a matrix form; the Fermi-Dirac distribution matrix is defined by,

$$\mathbf{f}_{FD}(E) = \tfrac{1}{2}[\mathbf{1}-\mathbf{\Sigma}^K(\mathbf{\Sigma}^C)^{-1}], \tag{18}$$

while, using Eq. (14), the density-of-states matrix at the node m and transverse mode l is expressed by

$$\mathbf{D}(lm:E) = \frac{ig_{sv}}{2\pi a}\boldsymbol{\Sigma}^C\mathbf{G}^A\mathbf{1}_{lm}\mathbf{G}^R. \tag{19}$$

Here, $g_{sv}=4$ is the spin-valley degeneracy, $\boldsymbol{\Sigma}^C=\boldsymbol{\Sigma}^R-\boldsymbol{\Sigma}^A$, and $\mathbf{1}_{lm}$ is a matrix whose elements are nonzero only at the lmth diagonal position. When the impurity scattering is absent, $\mathbf{f}_{FD}$ becomes the well-known results as in Ref. 11 and 16, where nonzero elements are only at $m=0$ and $m=M-1$ nodes and are equal to the Fermi-Dirac distribution characterized by μ_S and μ_D, respectively. However, due to the impurity scattering of $\boldsymbol{\Sigma}^{imp}$, elements of $\mathbf{f}_{FD}$ are deviated from the Fermi-Dirac distribution function in general.

Currents flowing through the device are defined by time derivatives of total charge at nodes $m=-1$ or $m=M$. Then, through the Heisenberg equation of motion, one can find that the currents become

$$I_{DS} = -\frac{e}{2\pi\hbar}\mathrm{tr}\,\Re\int_{-\infty}^{\infty}dE[\mathbf{G}^R\mathbf{1}_m\boldsymbol{\Sigma}^K\mathbf{1}_m + \mathbf{G}^K\mathbf{1}_m\boldsymbol{\Sigma}^A\mathbf{1}_m]$$
$$= -\frac{e}{2\pi\hbar}\mathrm{tr}\int_{-\infty}^{\infty}dE\mathbf{f}_{FD}(E)\mathbf{T}_m(E), \tag{20}$$

where, by $m=0$ or $M-1$, the expression means currents at the source or the drain, respectively, and $\mathbf{1}_m=\Sigma_l\mathbf{1}_{lm}$. In the second line of the above equation, we define the transmission matrix $\mathbf{T}_m$ by

$$\mathbf{T}_m = g_{sv}\boldsymbol{\Sigma}^C(\mathbf{1}_m\mathbf{G}^R\boldsymbol{\Sigma}^C\boldsymbol{\Sigma}^A\mathbf{1}_m - \mathbf{G}^A\mathbf{1}_m\boldsymbol{\Sigma}^C\mathbf{1}_m\boldsymbol{\Sigma}^R). \tag{21}$$

In the case of free impurities, this form also recovers the previous results.[11,16]

D. Approximations

Prior to numerical calculations, let us first look at the approximations used. Firstly, we consider a finite number N of transverse modes. Then, the solution of Eq. (14) is obtained by inverting a $(NM)\times(NM)$ matrix iteratively. However, this scheme demands the huge computational cost because the matrix size is large and is deviated from the tridiagonal form due to off-diagonal elements of the self-energy $\boldsymbol{\Sigma}$ and the Hamiltonian $\mathbf{v}$.

As an approximation, we consider leading terms in Green's functions to emphasize mainly the effects of the impurity scattering. This is equivalent to consider the diagonal components of the Green's functions for transverse modes. Namely, the coupling of different transverse modes in the self-energy $\boldsymbol{\Sigma}$ and the Hamiltonian matrix $\mathbf{v}$ are neglected. As indicated in Ref. 11, if the potential energy $U(\mathbf{r})$ is a slowly varying function along the radial direction at any node m the Hamiltonian matrix $\mathbf{v}$ becomes small and the approximation is well justified. As for the self-energy, leading terms in the Green's functions are obtained by writing overlap functions of Eq. (12) as

$$S_{lml'm:l_1ml_2m} \simeq \delta_{l_1l_2}\frac{u_0^2l_s^3}{2a}\langle\chi_l\|\chi_{l_1}(\rho)|^2n_D(\rho,z_m)|\chi_{l'}\rangle$$
$$\simeq \delta_{l_1l_2}\delta_{ll'}\frac{u_0^2l_s^3}{2a}\langle\chi_l\|\chi_{l_1}(\rho)|^2n_D(\rho,z_m)|\chi_l\rangle \tag{22}$$

and, therefore, the self-energy of Eq. (8) becomes diagonal for transverse modes. However, the approximation of Eq. (22) still couples transverse modes nontrivially because each diagonal component of the self-energy depends on others.

Another approximation is made in the Keldysh component of the impurity self-energy $\boldsymbol{\Sigma}^{imp,K}$. After various numerical calculations, we find that $\boldsymbol{\Sigma}^{imp,K}$ is well represented by

$$\boldsymbol{\Sigma}^{imp,K}_{lm:l'm'}(E) = \delta_{ll'}\delta_{mm'}\boldsymbol{\Sigma}^{imp,C}_{lm:lm}(E)$$
$$\times\begin{cases}\tanh\left(\dfrac{E-\mu_S}{2k_BT}\right) & \text{for } m < M/2\\ \tanh\left(\dfrac{E-\mu_D}{2k_BT}\right) & \text{for } m \geqslant M/2,\end{cases} \tag{23}$$

where a node $m=M/2$ is the middle point in the intrinsic Si wire. This indicates that particles at the nodes near the source(drain) have still the chemical potential μ_S (μ_D), not an intermediate value between μ_S and μ_D, even after suffering from scattering. We attribute this result to a particular potential distribution in the device of a source-to-channel barrier, which prevents particles with different chemical potentials from mixing.

III. RESULTS AND DISCUSSIONS

In this section, we numerically illustrate solutions of the nonequilibrium Green's functions suffering ionized-impurity scattering and related transport properties. We consider a typical case of the device structure which can be realized experimentally. As shown in Fig. 1, the source and drain regions are doped at $10^{20}/\mathrm{cm}^3$ and there is no gate-to-source and -drain overlaps to constitute nearly abrupt junctions with the intrinsic channel. The source and drain extensions are 15 nm each and the gate length L_G is 20 nm, so that a total device length simulated is 50 nm. By choosing a node spacing of $a=0.25$ nm, we have the number of 200 nodes along the wire. In order to claritfy the quantum effects, we choose a small radius (3 nm) of the wire which exhibits three mode occupancies at a zero temperature. However, to include thermally excited particles as well as the mode coupling from the impurity scattering, 20 transverse states are incorporated. The gate oxide layer has a thickness of 2.5 nm and is treated as an infinite potential barrier for electrons. Due to this, wave functions at the interface between the Si wire and the oxide are assumed to be zero in all of our simulation.

Poisson's equation is solved in the cylindrical coordinates with Dirchlet boundary conditions at the gate-oxide interface, otherwise, with Neumann conditions. For a rapid convergence of solutions, we use the Newton-Rhapson method for the Gummel form of external charges.[18] To model a gate material, we choose a work function of 4.56 eV, approximately for TiN.

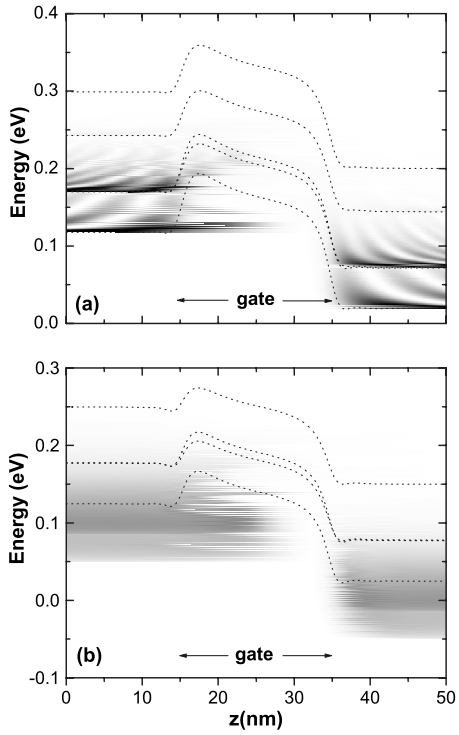

FIG. 2. For the cylidrical nanowire with $N_D=10^{20}/\mathrm{cm}^3$, $L_G=20$ nm, and $t_{ox}=2.5$ nm we plot calculated local local particle density as functions of energy and position for two cases of impurity scattering strengths of $u_0=0$ in (a) and 39 eV in (b), respectively. A darker color represents higher density. We also superimpose energies of subbands with dotted lines to show detailed built-in potential distributions. Calculations are performed at $V_{GS}=0.6$ V, $V_{DS}=0.1$ V, and $T=300$ K.

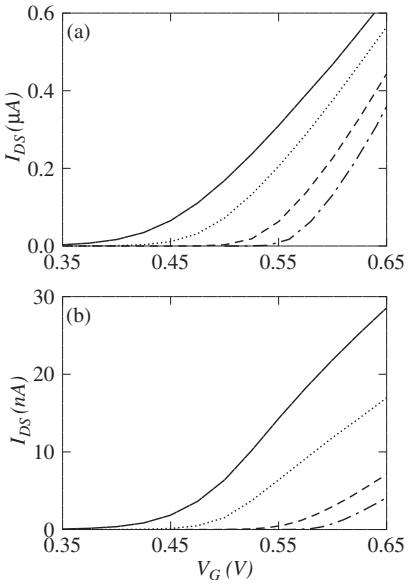

FIG. 3. We compare calculated I_{DS}-V_G results at temperatures of 300 K (solid), 200 K (dotted), 100 K (dashed), and 50 K (dot-dashed lines), respectively, for impurity-scattering strengths of $u_0=0$ in (a) and 39 eV in (b). Here, we assume a small source-drain bias of 0.02 V.

In Fig. 2, we show calculated electronic subbands of each level and local particle density along the wire, and compare the results with and without the impurity scattering in (a) and (b), respectively ($V_G=0.6$ V and $V_D=0.1$ V). The subband bottoms (dotted lines) reflect the calculated self-consistent potentials in which electrons at each levels feel at a node m. Regardless of the impurity scattering, they exhibit source-channel barriers. Since a high gate voltage lowers the energy barriers, the basic transistor action is achieved by controlling these barriers.[19]

The energy-resolved particle density is plotted in a gray scale; a darker area in the figure represents higher density. In the impurity-free case of (a), states injected from the drain-(source) end of the device undergo reflections and interfere strongly to the right(left) of the source-to-channel barrier because there is no momentum relaxation. This interference results in coherent oscillations in the particle density as seen in Fig. 2(a). It is found that the local particle density far from the source-channel barrier as a function of energy shows sharp peaks such as $1/\sqrt{E}$ at every onset of subbands, reminiscence of one-dimensional density of states.

If one turns on impurity scattering, phase information of the electrons within the device is randomized and the energy levels are renormalized. Above all, this makes the interference oscillations washed out in the local particle density as shown in Fig. 2(b). In addition, electronic states are shifted and broaden, so that the most electrons are found below subband bottoms and its occupation has no longer $1/\sqrt{E}$ dependence, but a monotonically varying function (the abrupt change of darkness along the energy direction comes from a different valley state). In both cases of the impurity scattering, one can see that electrons in the source and drain regions are well separated by the source-channel barriers from each other. Due to this, the approximation of Eq. (23) is justified with good accuracy.

In order to examine the electronic transport of the device, we calculate channel currents I_{DS} versus a gate voltage V_G at a small source-drain bias, and plot results in Figs. 3(a) and 3(b), respectively, with and without impurity scattering for several temperatures. Under this condition, currents exhibit rapidly increasing behavior as a gate voltage becomes larger. This shows the basic operation of a transistor as indicated in the previous section; the channel current turns on by lowing the source-channel barrier when a gate voltage is higher than a certain value, called a threshold voltage V_{th}. The increasing rate of channel currents as a function of a gate voltage is related to the substhreshold swings. We obtain the values of 62 and 68 mV/dec for the free and strong impurity cases, respectively, at 300 K. These values are comparable to the experimental one of 71 mV/dec in Ref. 6.

By comparing Figs. 3(a) and 3(b) at a given temperature, one can find that the presence of impurities reduces the currents significantly even though electrons in both cases are expected to move ballistically in the intrinsic gate region. This indicates that transport through the Si wire largely depends on the electronic structure of the source and drain regions.

As inspired by flat subbands in the figures, the potential drops across the intrinsic regions are nearly invariant to the impurity-scattering strength. Thus, it is reasonable to assume

that the suppressed currents do not come from the Fermi-Dirac matrix of Eq. (20) which crucially depends on the potential drop, but mainly from a reduced transmission coefficient of Eq. (21). One of possible explanations for this is that electrons injected from the source are partially reflected from impurities in the source extension in addition to that from the source-channel barriers and, thus electrons tunnel the source-channel barrier at rare intervals. This type of the reduction for the transmission coefficient is also encountered in problems of tunneling in dissipative environments.[20,21] According to the theories, when environments of the device become more dissipative, carriers are harder to tunnel the barriers because more energies should be transferred to the environment.

As a function of a temperature, curves show similar profiles except the shifting to larger values and slightly different slopes in both cases of the impurity scattering. Two points are noteworthy. Firstly, the threshold voltage is shifted to a higher value as a temperature is lowered. This is easily understood because as the temperature decreases, available electrons to overcome source-to-channel barrier thermally are reduced and then more potential energy should be supplied electrostatically to turn on currents. Secondly, we look at the slopes of the I_{DS}-V_G curves. In conventional metal-oxide field-effect transsistors (MOSFETs), they are related to a channel mobility μ_m via a relation of $I_{DS} \propto \mu_m (V_G - V_{th}) \times (V_D - V_S)$. As seen in the figures, our results show linear behavior in some range of gate voltages. Therefore, we may understand the slopes to be proportional to the mobility of electrons in the device. For detailed comparison, we define the conductance by

$$\sigma(T) = \left. \frac{\partial I_{DS}}{\partial V_G} \right|_{V_G = 0.65 \text{ V}}, \tag{24}$$

known as the transconductance in MOSFETs.

Calculated conductance is summarized in Fig. 4 as a function of impurity-scattering strength and temperature. In Fig. 4(a) we compare the conductance with increasing impurity-scattering strength for two temperatures. It is noted that the conductance decreases monotonically when the impurity-scattering strength becomes larger at both temperatures and, consequently, suppressed mobilities are expected. In Fig. 4(b) we plot the temperature dependence of the conductance for various impurity-scattering strengths. For a bulk material, it is well known that the mobility resulted from impurity scattering is proportional to $T^{3/2}$ to the first order (dotted line in the figure).[22] In the case of a two-dimensional system, the ionized-impurity scattering (for instance, in a quantum well with a δ doping) is enhanced due to the increased overlap of the ionized impurity with electron wave functions and the mobility decreases nearly exponentially when a temperature is lowered (dashed line).[23] In our case of a quasi-one-dimensional system, the conductance shows different temperature dependences from those of higher-dimensional ones; the conductance of the Si wire interpolates from linearly increasing behavior of the impurity-free case to the exponentially decaying dependence of a strong impurity scattering as a function of scattering strength. Curves shown in Fig. 4(b) do not provide a definitive comparison of ionized-impurity scattering among three different dimensional systems because each system has different doping profiles and concentrations. Despite this, it is interesting to note that the ionized-impurity scattering becomes less temperature dependent when the system has a lower dimension.

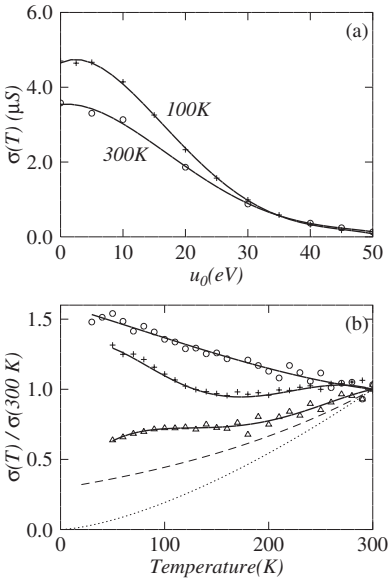

FIG. 4. In (a), we plot calculated conductances(symbols) as a function of impurity-scattering potential at two different temperatures of 300 and 100 K, respectively (V_D=0.02 V). In (b), calculated conductances are plotted as a function of temperature for given impurity-scattering potential of u_0=0 (circles), 23 eV (crosses), and 39 eV (triangles), respectively. Solid lines are just guide to the eyes. To emphasize their temperature dependence we normalize them with values at 300 K and superimpose the lines of $e^{1.22(T/300\text{ K}-1)}$ (dashed) and $(T/300\text{ K})^{3/2}$ (dotted).

IV. SUMMARY

In summary, we study transport through a gate-surrounded Si wire in the ballistic regime by considering the ionized-impurity scattering. Using the Schwinger-Keldysh approach, we include the impurity scattering within the self-consistent Born approximation and present expressions for electron densities and current in terms of nonequilibrium Green's functions and self-energies. By simulating a typical case of a Si wire, we compare electron densities and channel currents for zero- and strong-impurity scattering strengths. In the case of the strong-impurity scattering, we find that the local particle density profiles are shifted and broaden to result in suppressed currents compared to the zero-impurity scattering case, and the oscillating interference pattern vanishes. Calculated currents and conductances are also presented as functions of temperature and the impurity-scattering strength. It is found that the conductance of a Si wire exhibits various behaviors by decreasing temperature, which interpolate from a linear increasing function at a zero scattering to an exponentially decreasing function for the strong scattering case. However, in this work, we do not

include other inelastic scattering processes such as acoustic and optical phonon scatterings which will be occurred in real devices. Therefore, our results show the effects of the ionized-impurity scattering alone on electronic transport through a Si wire.

ACKNOWLEDGMENTS

The authors would like to thank M. Shin for useful discussions. This work was supported by the Korean Ministry of Science and Technology through the Creative Research Initiatives Program under Contract No. R17-2007-010-01001-0(2007).

APPENDIX: GREEN'S FUNCTIONS OF A UNIFORMLY DOPED WIRE

In this appendix, we illustrate Green's functions for an infinitely long Si wire which is doped uniformly. Eigenstates are plain waves whose wavelength is determined by periodic boundary conditions. Since the wire is translational invariant, the self-energy in Eq. (8) is independent of a longitudinal position. Then, the retarded component of the Green's function can be derived as

$$\mathbf{G}^R_{lm:l'm'}(E) = \frac{\delta_{ll'}}{M_0} \sum_{k=-M_0/2}^{M_0/2} \frac{e^{2\pi ik(m-m')/M_0}}{E - \epsilon_{lk} - \mathbf{\Sigma}^{imp,R}_{lm:l'm'}(E)}, \quad \text{(A1)}$$

where M_0 is the number of a longitudinal node and $\epsilon_{lk}=\epsilon_l + 2t_H[1-\cos(2\pi k/M_0)]$ with an eigenenergy ϵ_l of the lth transverse mode. In the limit of a large M_0, diagonal components of the Green's function read

$$\mathbf{G}^R_{lm:lm}(E) = \frac{1}{4t_H} \frac{\mathrm{sgn}[y_l(E) - 1/2]}{\sqrt{y_l^2(E) - y_l(E)}}, \quad \text{(A2)}$$

with

$$y_l(E) = \frac{E - \epsilon_l - \mathbf{\Sigma}^{imp,R}_{lm:lm}(E)}{4t_H}$$

and, according to Eqs. (8) and (22), the self-energy is proportional to the diagonal component of the Green's functions such as

$$\mathbf{\Sigma}^{imp,R}_{lm:l'm'}(E) = \delta_{mm'}\delta_{ll'} \sum_{l_1} S_{lmlm:l_1m:l_1m} \mathbf{G}^R_{l_1m:l_1m}. \quad \text{(A3)}$$

Thus, the Green's functions are obtained by solving Eqs. (A2) and (A3) self-consistently. On the other hand, the chemical potential μ_0 of the uniformly doped wire can be found from the particle density of $n_{lm}=-g_{sv}\Im\mathbf{G}^R_{lm:lm}(E)/\pi a$ together with Poisson's equation.

The self-energy of Eq. (12) caused by the coupling of the device to the source and drain regions is obtained by solving the uniformly doped wire with vanishing boundary conditions. In the similar way to Eq. (A2), it is given by

$$\tilde{\mathbf{\Sigma}}^R_{lm:l'm}(E) = \delta_{ll'}t_H[2y_l(E) - 1]\left\{1 - \sqrt{1 - \frac{1}{[2y_l(E) - 1]^2}}\right\}. \quad \text{(A4)}$$

*dahn@uos.ac.kr

[1] T. J. Thornton, M. Pepper, H. Ahmed, D. Andrews, and G. J. Davies, Phys. Rev. Lett. **56**, 1198 (1986).
[2] K. K. Choi, D. C. Tsui, and S. C. Palmateer, Phys. Rev. B **32**, 5540 (1985).
[3] B. J. van Wees, H. van Houten, C. W. J. Beenakker, and J. G. Williamson, L. P. Kouwenhoven, D. van der Marel, and C. T. Foxon, Phys. Rev. Lett. **60**, 848 (1988).
[4] L. DiCarlo, Y. Zhang, D. T. McClure, D. J. Reilly, C. M. Marcus, L. N. Pfeiffer, and K. W. West, Phys. Rev. Lett. **97**, 036810 (2006).
[5] K. Nishiguchi and S. Oda, Appl. Phys. Lett. **76**, 2922 (2000).
[6] K. H. Cho, Y. C. Jung, B. H. Hong, S. W. Hwang, J. H. Oh, D. Ahn, S. D. Suk, K. H. Yeo, D. Kim, D. Park, and W. S. Lee, Appl. Phys. Lett. **90**, 182102 (2007); K. H. Cho, S. D. Suk, Y. Y. Yeoh, M. Li, K. H. Yeo, D. Kim, S. W. Hwang, D. Park, and B. Ryu, Tech. Dig. - Int. Electron Devices Meet. **2006**, 543.
[7] M. V. Fernandez-Serra, Ch. Adessi, and X. Blase, Phys. Rev. Lett. **96**, 166805 (2006); M. V. Fernandez-Serra, Ch. Adessi, and X. Blase, Nano Lett. **6**, 2674 (2006).
[8] J. Masek, Z. Phys. B: Condens. Matter **64**, 145 (1986).
[9] Ben Yu-Kuang Hu and S. Das Sarma, Phys. Rev. B **48**, 14388 (1993); H. Sakaki, Jpn. J. Appl. Phys. **19**, L735 (1980).
[10] R. Venugopal, M. Paulsson, S. Goasguen, S. Datta, and M. S. Lundstrom, J. Appl. Phys. **93**, 5613 (2003).
[11] J. Wang, E. Polizzi, and M. Lundstrom, J. Appl. Phys. **96**, 2192 (2004).
[12] A. Kamenev and A. Andreev, Phys. Rev. B **60**, 2218 (1999).
[13] H. E. Camblong and P. M. Levy, Phys. Rev. Lett. **69**, 2835 (1992).
[14] R. Lake, G. Klimeck, R. C. Bowen, and D. Jovanovic, J. Appl. Phys. **81**, 7845 (1996).
[15] M. Diarra, Y. M. Niquet, C. Delerue, and G. Allan, Phys. Rev. B **75**, 045301 (2007).
[16] S. Datta, *Electronic Transport in Mesoscopic Systems* (Cambridge University Press, Cambridge, 1997).
[17] J. H. Oh, D. Ahn, and S. W. Hwang, Phys. Rev. B **72**, 165348 (2005).
[18] H. K. Gummel, IEEE Trans. Electron Devices **11**, 455 (1964); M. Shin (private communication).
[19] E. O. Johnson, RCA Rev. **34**, 80 (1973).
[20] J. H. Oh, D. Ahn, and S. W. Hwang, Phys. Rev. B **68**, 205403 (2003).
[21] G. Ingold and Y. V. Nazarov, in *Single Charge Tunneling*, edited by H. Grabert and M. H. Devoret (Plenum, New York, 1992).
[22] R. A. Smith, *Semiconductors* (Cambridge University Press, Cambridge, 1978).
[23] W. T. Masselink, Phys. Rev. Lett. **66**, 1513 (1991).